PROCEEDINGS, 42nd Workshop on Geothermal Reservoir Engineering
Stanford University, Stanford, California, February 13-15, 2017
SGP-TR-212

Finite-Element Modelling of Wellbore-Observed Fracture-Borne Heat Advection – Application to EGS Stimulation in Basement Rock

Peter Leary, Peter Malin & Rami Niemi

St1 Deep Heat Ltd, Purotie 1, 00380 Helsinki, Finland

p.leary@auckland.ac.nz

Keywords: EGS, fractures, scaling, wellbores, porosity, permeability, stimulation, fluid flow, advection, finite element modelling

ABSTRACT

Wellbore logs of neutron porosity φ and thermal gradient T_z recorded in a western Colorado tight gas sandstone reservoir formation are observed to be 65% correlated over a 500-meter interval containing conspicuous fracturing. The strong φ-T_z spatial correlation can be understood in terms of a regional groundwater heat transport system locally transected by a series of fracture intervals with elevated porosity and associated increased permeability leading to an anomalous temperature distribution associated with fracture-connectivity fluid conduits. We compute the observed temperature phenomenology for advective fluid flow in fractures embedded in an otherwise stochastically uniform crust, and apply the heat transport model to fracture-connectivity flow to an EGS wellbore-to-wellbore flow stimulation scenario at depth in Finnish basement rock.

Fluid flow in crustal rock and hosted fracture sequences is characterised by a trio of empirical rules attested across a wide range geological settings. For crustal fluid flow systems of either conventional and unconventional oil/gas, geothermal or ground waters, or fossilized-flow mineral deposits, the spectral power of well-log spatial fluctuations, most particularly that of porosity φ, is observed to scale inversely with spatial frequency, $S(k) \sim 1/k^{\beta}$, where $\beta \sim 1$ over 5 decades of scale length $1/\text{cm} < k < 1/\text{km}$. Over the same range of geological settings, well-production of crustal fluids is observed to be lognormally distributed as described by well-scale permeability distribution $\kappa \sim \kappa_0 \exp(\alpha\varphi)$ for porosity $0 < \varphi < 1$ and scale parameter $20 < \alpha < 50$; the magnitude of parameter α guarantees a lognormal distribution of flow system permeability for a normal distribution of porosity. Spatial fluctuation sequences of well-core porosity δφ and the logarithm of well-core permeability δlog(κ) from hydrocarbon and geothermal reservoirs are observed to be highly correlated, $\Gamma(\delta\varphi, \delta\log(\kappa)) \sim 70\%\text{-}85\%$.

The trio of crustal flow system empirics are attested for the tight gas sand formations hosting the φ-T_z spatial correlation. Neutron porosity well-log fluctuation power-spectra scale inversely with spatial frequency, $S(k) \sim 1/k^{1.17}$. Well-core porosity and permeability sequences are ~ 80% spatially correlated. Regional gas-field well-productivities are lognormally distributed. For reasonable assumptions of regional crustal structure and properties, the spatial correlation between wellbore temperature gradient fluctuations δT_z and neutron porosity fluctuations δφ can be expressed as $\delta T_z \approx P_e(T - T_0)/h\ \delta\varphi$, for thermal advection Peclet number $P_e \equiv C\rho^2 g\kappa h/K\mu$. With $P_e \sim 5$, wellbore interval temperature $T - T_0 \sim 50^{\circ}\text{C}$, vertical flow system scale $h \sim 0.850\text{km}$, and neutron porosity spatial fluctuations $\delta\varphi \sim 30\%$, temperature gradient fluctuations of order $\delta T_z \sim 100^{\circ}\text{C/km}$ accord with observation.

The observed temperature distribution is computed for a 2D crustal section by applying the fluid-rock interaction empirics to the observed porosity distribution. With local permeability fixed by local porosity, $\kappa \sim \kappa_0 \exp(\alpha\varphi)$, conservation of mass $\nabla\cdot(\kappa\nabla P) = 0$ in a closed flow system fixes the model pressure $P(x,z)$ to give Darcy flow velocity $v(x,z) = \kappa(x,z)/\mu\ \nabla P(x,z)$. Fluid flow in the model section is divided between low poroperm flow in the ambient crust and high poroperm flow in the fractures. Conservation of thermal energy $\partial_t T = D\ \nabla\cdot(\nabla T - \eta T v)$ fixes the temperature field for fluid velocity $v(x,y)$ with rock thermal diffusivity $D \sim 1.5\ 10^{-6}\ \text{m}^2/\text{s}$ and the ratio $\eta \equiv C_w\rho_w/C_r\rho_r \sim 2$ of volumetric heat capacities of water and rock. A 2D finite-element solver for $\partial_t T = D(\nabla^2 T - \eta\nabla T\cdot v)$ reproduces the observed φ-T_z spatial correlation for plausible fluid flow in the fractures.

Crustal fracture/fluid-flow empirics allow the observed wellbore φ-T_z spatial correlation to serve as a template for wellbore-to-wellbore fluid flow in an EGS crustal heat-exchange volume. Advective heat transport analogues computed for input and outtake wells in a EGS stimulation volume indicate it is plausible for high wellbore pressurization to activate wellbore-centric thermal advection Peclet number $P_e \sim 5$ flow in basement rock of porosity levels $\varphi \sim 1\%$ with $\kappa_0 \sim 1\mu\text{D}$ base permeability. It is possible that wellbore pressurization reactivates relic permeability pathways attested by high degrees of neutron scattering from the hydrated mineral content of basement rock.

1. INTRODUCTION

M King Hubbert (1940, 1941, 1956) envisioned putting Darcy's law of groundwater flow onto a rigorous physical and mathematical footing. Recognizing that surface observers can only infer how groundwater flows in geological formations, he sought to impose mathematical and physical order on physical processes that we cannot directly observe. Hubbert's attempt to impose order on groundwater studies has proved, however, to be deeply flawed. With the advantage of present-day observations and modelling resources of finite element computation, we can bypass earlier misapprehensions about crustal permeability to advance our understanding and management of crustal fluid flow. In particular, we can bring more accurate physical perspectives to the difficult task of enhancing crustal permeability between wellbores for commercially viable heat extraction.

1.1 Hubbert & formation permeability

Hubbert focused on making an analogy between Darcy's proportionality relation for pressure-gradient and groundwater flow velocity, $\boldsymbol{v} \propto \nabla P$, and the gradient flow laws of Fourier for heat ($\boldsymbol{Q} = K\nabla T$), Ohm for electrical current ($\boldsymbol{J} = \sigma\nabla V$), and Fick for chemical diffusion ($\boldsymbol{M} = D\nabla C$). To impose this analogy on groundwater flow, Hubbert accepted the view of permeability for geological materials adopted by Darcy (1856) and Dupuit (1863) from their work with filtration flow through unconsolidated sands. Citing Muskat's 1937 treatise on fluid flow in porous media, Hubbert (1940) views crustal permeability as a function of the specific granular nature of a given geological formation. In his 1941 address to the New York Academy of Sciences, Hubbert combined conservation of mass with conservation of energy to conclude that groundwater flow within a geological formation followed smooth streamlines defined by gravitational potential. His 1956 celebration of the Darcy centennial introduced a sketch, reproduced as Fig 1, by which to 'derive' Darcy's law from the Navier-Stokes equations. The Fig 1 sketch asserts that averaging over grain-scale spatial fluctuations in porosity produces an 'effective medium' continuum approximation to *in situ* permeability. Significant changes in Fig 1 groundwater porosity distributions occur only with changes in geological formation at the largest scales.

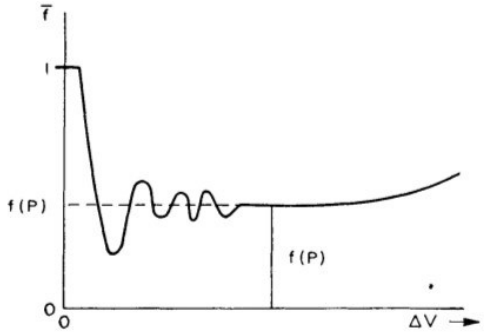

FIG. 5 — Method of defining point values of macroscopic quantities illustrated with the porosity *f*.

Figure 1: Schema of Hubbert (1956) illustrating the idea that significant spatial fluctuations at small scales (plot left) are effectively averaged over to produce a quasi-uniform 'effective medium' continuum (dashed line) at all scales smaller than formation dimension scales (plot right).

In mathematical terms, Hubbert's Fig 1 hypothesises 'spatial order', meaning that Darcy's groundwater flow velocity vector $\boldsymbol{v}$ is proportional to the pressure fluid vector gradient via the essentially constant fluid viscosity μ and an 'effectively uniform' formation permeability κ_{eff} valid at all scales,

$$\boldsymbol{v} = \kappa_{eff}/\mu \, \nabla P. \tag{1}$$

A signature feature of (1) follows from conservation of mass in steady-state flow that requires the divergence of the Darcy velocity to vanish,

$$\nabla \cdot \boldsymbol{v} = 0. \tag{2}$$

If we accept Fig 1 spatial order, constraint equation (2) yields the highly convenient standard mathematics of potential theory by which to interpret groundwater pressure data,

$$\nabla \cdot \nabla P = \nabla^2 P = 0. \tag{3}$$

If, however, we choose not to accept Hubbert's Fig 1 spatial order and allow permeability to be disordered by varying within geological formations, conservation of mass applied to Darcy flow gives (for constant fluid viscosity μ) the more complex expression,

$$\nabla \cdot (\kappa \nabla P) = \kappa \nabla \cdot \nabla P + \nabla \kappa \cdot \nabla P = 0. \tag{4}$$

Expression (4) enters territory into which Hubbert did not choose to venture. Imposing Fig 1 on (4) to render permeability gradients $\nabla\kappa$ negligible within geological formations eliminates a range of possible difficulties for groundwater studies.

Formal or informal acceptance of Hubbert's Fig 1 groundwater permeability sketch extended from contemporary groundwater flow treatments (Theis 1935; Muskat 1937; Biot 1941; Jacob 1946; Horner 1951) to developments by Hantush & Jacob (1954) and deWiest (1961, 1966), the introduction of the 'representative elementary volume' by Bear (1972), to more recent treatments of fluid flow in the crust (e.g., Freeze 1975; Earlougher 1977; Gelhar 1986; Bachmat & Bear 1987; Yeh & Stephens 1988; Ingebritsen, Sanford & Neuzil 2006; Nordahl & Ringrose 2008; Costanz-Robinson, Estabrook & Fouhey 2011).

It happens, however, that permeability in geological formations does not conform to Hubbert's Fig 1 vision of spatially-averaged 'effective medium' continua. A vast range of well-log, well-core, and well-productivity data for crustal fluids in many geological and tectonic settings systematically shows that formation porosity and permeability, along with the gradient term $\nabla\kappa$ in (4), are spatially

highly variable within and without individual formations at scale lengths from cm to km. Such spatial variability has a great deal to say about what happens to the flow of groundwater and other crustal fluids across a wide range of rock types for a wide range of porosity and permeability. In particular the $\nabla\kappa$ term in (4) has a large impact on EGS crustal permeability stimulation and heat energy production.

1.2 Reformulating formation permeability -- Well-log, well-core and well-production empirics

Well-log, well-core, and well-productivity data to all drillable depths worldwide show that random spatial fluctuations of porosity and permeability within and between geological formations are spatially correlated at all scale lengths from cm to km, and that the spatial fluctuation amplitudes systematically increase with increasing scale length (Leary 1991, 1997, 2002; Leary & Al Kindy 2002; Leary et al 2015; Malin et al 2015; Pogacnik et al 2015). In direct opposition to Fig 1, spatial averages of fluid flow properties in the crust tend to vary strongly at all spatial scales rather than follow a natural tendency to quasi-uniformity that eliminates spatial variability as a physical feature.

Due to long-range spatially correlated randomness in crustal rock, geological formations can host large-scale spatially-erratic fluid flow pathways which dominate the formation flow structure but cannot be detected as such by traditional sparse small-scale sampling methods. Further, random spatial fluctuations of porosity and permeability in geological formations can override formation geometry. It follows that applying standard potential theory methods (3) to characterizing flow within a crustal volume is often largely irrelevant. New approaches allowing for spatial heterogeneity term $\nabla\kappa$ in (4) are required to understand and manage the flow of groundwater and other crustal fluids.

Two resources are at hand to solve for the spatial complexities represented by the $\nabla\kappa\cdot\nabla P$ term in (4). First, widely available finite element computational methods are fundamentally suited to the task of handling complex differential equations (Hughes 2000; Hjelmstad 2005). Second, multichannel seismic data recording and processing can provide basic flow spatial complexity structure information by locating weak seismic emissions generated by spatially coherent flow structures in crustal volumes (Geiser, Lacazette, Vermilye 2012; Malin et al 2015). Direct-observation flow-structure data combined with finite element modelling can solve the general constraint equation (4). It is plausible that wellbore-based stimulation of formation fluids to generate seismic signals within complex formation permeability structures is both necessary and sufficient to move beyond Hubbert's Fig 1 spatial averaging perspective.

A general perspective crustal fluid flow spatial complexity emerges from applying (4) to a pair of empirical relations characterizing formation porosity φ and permeability κ. One empirical relation arises from well-core phenomenology $\delta\varphi \sim \delta\log(\kappa)$ that directly relates porosity to the logarithm of permeability (Leary & Al Kindy 2002; Pogacnik et al 2015), Integrating this well-core-scale fluctuation relation to the scale of reservoir formations spanned by well-core sequences gives the expression

$$\kappa \approx \kappa_0 \, exp(\alpha(\varphi-\varphi_0)), \tag{5}$$

with α a constant of integration to be empirically determined. Observed values of α are typically 20-40 for crustal reservoir formations with porosity $\varphi \sim 0.1$-0.3 (Malin et al 2015; Pogacnik et al 2015). In §2 below tight gas sands well-core data with porosity $\varphi \sim 0.1$ are seen to support $\alpha \sim 24$, while well-core data from low porosity basement rock with $\varphi \sim 0.01$ support $\alpha \sim 300$.

With well-core poroperm empirics indicating that the argument of (5) is of order $\alpha\varphi \sim 2$-3, we observe that, as crustal porosity is generally normally distributed, (5) implies that crustal permeability is generally lognormally distributed. The greater the value of empirical parameter α, the greater the lognormal skew of the associated permeability distribution. Lognormal crustal flow distributions consistent with (5) for empirical values of α are observed worldwide for all types of crustal fluid systems: Law 1944, Warren & Skiba 1964; USEIA 2011 for conventional oil/gas fields; IEA 2012 for unconventional oil/gas fields; IFC 2013 for geothermal fields; Gustafson 2002 and Banks et al 2010 for basement rock groundwater aquifers; de Wijs 1951, 1953 and Krige 1951 for fossil flow aqueous mineral deposits.

Lognormality of crustal flow system distributions (5) implies that the empirical parameter α quantifies the degree to which spatially-correlated formation porosity links create spatially varying flow paths within formations. Substituting (5) into (4) gives form to this inference via the conservation of mass constraint equation in which spatial variations in fluid pressure is directly related to spatial variation in porosity,

$$\nabla^2 P + \alpha\nabla\varphi\cdot\nabla P = 0. \tag{6}$$

The spatial correlation nature of porosity present in (6) follows from the second empirical characteristic of crustal flow systems. For a wide range of geological environments (Leary 1991; 1997; 2002), well-log spatial sequences for neutron porosity, sonic velocity, electrical resistivity, gamma activity, and chemical abundances are observed to have a fixed Fourier power-spectral trend in which fluctuation power $S(k)$ scales inversely with spatial frequency k over five decades of scale length,

$$S(k) \sim 1/k^{\beta}, \;\; 1 < \beta < 1.2, \quad 1/\text{km} < k < 1/\text{cm}. \tag{7}$$

The spatial connectivity nature of fluid flow empirics (5)-(7) for a 2D crustal section is illustrated in Fig 2 by finite-element solutions of (6) for different values of α in (5) combined with the equation (7) spatial correlation nature of porosity. Fluid flow patterns are realised for flow in a plane between two wells; the embedding flow medium has normally distributed stochastic porosities in the range $\varphi \sim 0.1$-0.3.

Fig 2 upper panels show flow distributions computed for spatially uncorrelated random porosity ('white noise') characterised by flat power spectra $S(k) \sim 1/k^{\beta}$, $\beta = 0$, for two values of $\alpha = 3$ and 10. The quasi-uniform spatially-averaged flow patterns generated by low values of spatial correlation parameters correspond to Hubbert's Fig 1 spatial-averaging hypothesis. In contrast, Fig 2 lower panels show flow channeling due to higher values of $\alpha \sim 20$-40 applied to spatial correlations generated by $\beta \sim 1$.

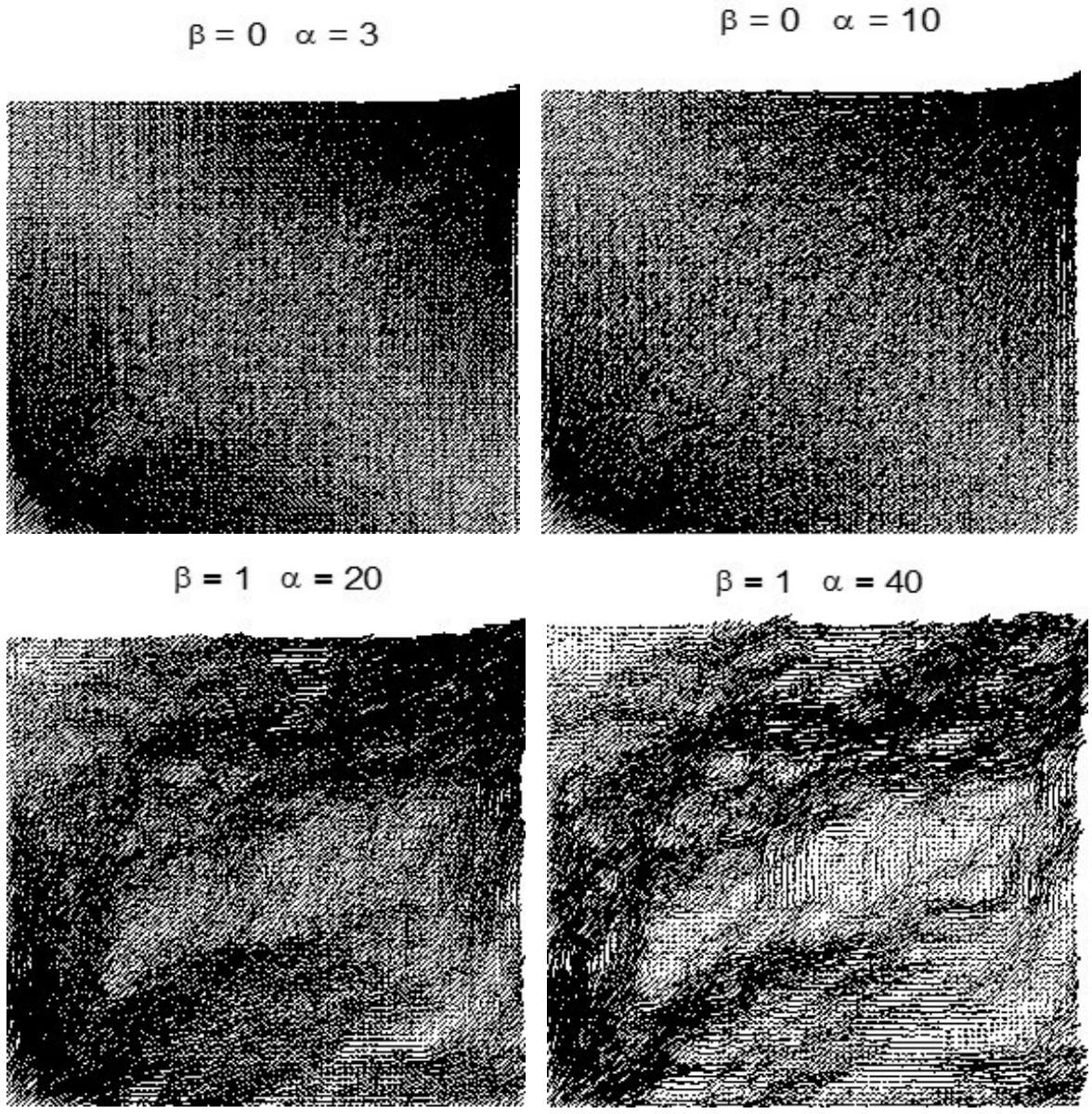

Figure 2: Wellbore-to-wellbore flow sections in poroperm medium of porosity range $\varphi \sim 0.1$-0.3. Upper panels show flow heterogeneity character for low degrees of porosity spatial correlation, $\beta \sim 0$, $\alpha \sim 3$-10, consistent with Hubbert's Fig 1 spatial averaging sketch. Lower panels show flow heterogeneity character for higher degrees of porosity spatial correlation, $\beta \sim 1$, $\alpha \sim$ 20-40, that are observed worldwide. Lower panel macroscopic flow channels arise from spatially correlated porosity and associated degrees of poro-connectivity characteristic of the actual crust; well-production from channeled flow is lognormally distributed. Little field evidence exists for the upper-panel quasi-uniform 'effective medium' continuum flow distributions hypothesized in Fig 1.

The channeled flow patterns of the Fig 2 lower panels create the lognormal well-production distributions (5) characteristic of actual crustal formations for crustal fluids in general. Within crustal reservoirs, only wells intersecting large-scale flow channels are highly productive; wells not intersecting high-correlation flow channels are less productive. The flow-channeling perspective extends to fluid flow in low-porosity crystalline rock. Fig 5 well-core poroperm data below show that lower values of porosity are associated with higher values of α, hence Fig 2 flow channeling characterises fluid flow heterogeneity relevant to EGS stimulation.

Spatial correlation spectral scaling (7) admits of a third characteristic exponent, $\beta \sim 2$. The higher value of spectral scaling exponent realises the hypothesis that layers or blocks of distinct uniform geological formations control the spatial distribution of fluid flow in the

crust. Highly correlated spatial randomness – for which grain-scale properties are statistically similar except at interfaces at which discrete jumps in statistical properties occur – generates spatial-fluctuation power spectra that scale inversely with the square of spatial frequency, $S(k) \sim 1/k^{\beta}$, $\beta \sim 2$. The empirical spatial fluctuation property of geological media, $\beta \sim 1$, is thus seen to fall exactly between the spectral-scaling extremes of minimum spatial correlation ($\beta \sim 0$) and maximal spatial correlation ($\beta \sim 2$). Empirical data demonstrating that long-range spatial correlation processes, $\beta \sim 1$, exist at all scales in all geological formations, comprehensively eliminate the Fig 1 hypothesis of uniform fluid flow in spatial averaged uncorrelated property fluctuations, $\beta \sim 0$, except at the largest scales where distinct geological formations control fluid flow through having different uniformly-distributed spatially-averaged flow properties, $\beta \sim 2$.

1.3 Thermal energy transport coupled to fluid flow

The universal nature of well-log, well-core, and well-production empirics invites application of Fig 2 to EGS wellbore pressurisation for enhanced permeability in crystalline rock. The standard view of EGS translates the Fig 1 sketch of crustal property variation into the Fig 3 sketch of permeability stimulation (Tester et al 2006). By Fig 1/Fig 3, wellbore pressurisation fluids cleave essentially uniform rock formation continua into predictable planar slabs (e.g., Warren & Root 1963; Hubbert & Willis 1957; Gringarten & Witherspoon 1973; Wunder & Murphy 1978). EGS experience to date shows, however, that wellbore-stimulation is far less controlled and regular than expected from Fig 3 (e.g., Parker 1989; Shapiro & Dinske 2009; Hasting et al 2011; Cladouhos et al 2015). The observed erratic EGS stimulation response to wellbore fluid pressurization is consistent with the Fig 2 lower-panel view of crustal rock being pervaded at all scale lengths by the spatially unpredictable and erratic long-range spatially-correlated flow channels with empirical parameters $\beta \sim 1$ and $\alpha \sim$20-40 for porosity φ in range 0.1-0.3 and $\alpha \sim 300$ for porosity $\varphi \sim 0.01$.

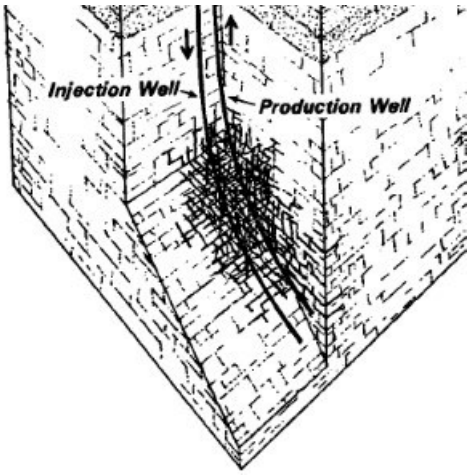

Figure 3: Schema of wellbore-to-wellbore flow stimulation assuming that crustal rock cleaves in regular planar sections providing predictable flow paths between input and outtake wellbores (Tester, Brown & Potter 1989). According to Tester et al (2006), *The heat-transfer system can be thought of as…a series of flat plates with gaps (the fractures) between them… Heat is transferred by conduction...perpendicular…to the fractures.* This view is consistent with the Fig 1 effective uniformity in poroperm properties associated in Fig 2 with spatial correlation parameter values $\alpha \sim$3-10 and $\beta \sim 0$. Such values are not observed in actual rock.

Understanding EGS measures in actual rock requires adapting thermal advection computation to spatially-correlated fluid flow structures $v(x,y,z)$ represented in the lower panels of Fig 2. Conservation of thermal energy, $C_r\rho_r\partial_t T = \nabla\cdot(K\nabla T - C_w\rho_w T\boldsymbol{v})$, couples the spatially-variable temperature field to the spatially-variable heat transport fluid velocity flow field. For EGS flow, we may reduce the spatial-correlation flow problem from 3D to 2D appropriate to wellbore-centric flow geometries in which fluid flow and heat transport occur in radial planes between two parallel wellbores. For essentially constant thermal properties for water and rock, rock thermal conductivity K and volumetric heat capacities $C_w\rho_w$ and $C_r\rho_r$ give constant rock thermal diffusivity $D \equiv K/C_r\rho_r \sim$ 3W/m·°C/840J/kg·°C/2400km/m^3 ~ 1.5 10^{-6} m^2/s and constant heat capacity ratio $\eta \equiv C_w\rho_w/C_r\rho_r \sim$ 4280J/kg·°C/1000kg/m^3 /(840J/kg·°C/2400kg/m^3) ~ 2. Wellbore-centric 2D thermal advection in a rock medium of spatially heterogeneous poroperm properties is then governed by the energy conservation condition,

$$\partial_t T(x,y,t) = \nabla\cdot[D\nabla T(x,y,t) - \eta T(x,y,t)\, \boldsymbol{v}(x,y)]. \quad (8)$$

Eq (8) has analytic utility in the approximation of uniform radial flow in or out of wellbores, $v(r) \sim r_0 v_0/r$. With radial component divergence operator $\nabla\cdot\mathbf{A}(r) = 1/r\, \partial_r(rA_r)$ and system parameter $P_e \equiv r_0 v_0/D$, (8) becomes

$$\partial_t T(r,t) = D\,[\partial_r{}^2 T(r,t) + (1 - \eta P_e)/r\, \partial_r T(r,t)]. \quad (9)$$

In (9) $P_e \equiv r_0 v_0/D$ is the wellbore-centric radial heat advection Peclet number given by the ratio of advected heat flow $r_0 v_0$ to thermal conduction heat flow parameter D. The role of heat advection embodied in P_e emerges from the analytic solutions $T(r,t)$ for (9). Steady-state advective flow $T_{ss}(r)$ for advective radial flow between inner radius r_0 at temperature T_0 and outer radius r_1 at temperature T_1 is

$$T_{ss}(r) = T_0 + (T_1 - T_0)((r/r_0)^{Pe} - 1)/((r_1/r_0)^{Pe} - 1). \quad (10)$$

Time-evolving temperature solution $T(r,t)$ proceeds from Laplace transforming (9) (Carslaw & Jaeger 1959, §15.2). For a line-source heat pulse of energy Q joules per length, the time-evolving temperature field is controlled by wellbore-centric Peclet number as $\gamma \equiv P_e/2$,

$$T(r,t) = Q/4\pi Kt\Gamma(\nu+1)\ (r^2/4Dt)^{\gamma}\ exp(-r^2/4Dt),$$

with $\Gamma(\nu+1)$ the gamma function of argument $\nu+1$. The corresponding solution for advective flow from a line source of radius a at temperature T_0 into an infinite medium initially at temperature zero is

$$T(r,t) = T_0 + 2/\pi \cdot T_0 \cdot (r/a)^{\gamma} \cdot \int dk/k\ exp(-k^2 Dt) \cdot [J_{\gamma}(kr)Y_{\gamma}(ka) - Y_{\gamma}(kr)J_{\gamma}(ka)]/[J_{\gamma}^2(ka) + Y_{\gamma}^2(ka)]. \quad (11)$$

Numerical solutions of advective heat transport coupling Eq (9) allows in principle obtaining a radial-plane fluid velocity field $\boldsymbol{v}(x,y)$ in terms of an observed radial-plane thermal field $T(x,y,t)$ or a radial-plane thermal field $T(x,y,t)$ in terms of an observed radial-plane fluid velocity field $\boldsymbol{v}(x,y)$. We explore finite-element solutions to (5)-(9) for both cases of wellbore-sourced flow and temperature data:

- Observed wellbore axial temperature-gradient data in sandstone formations connected to modelled groundwater flow for a well-log documented fracture-system intersecting the wellbore;
- Thermal heat extraction computed for hypothetical EGS flow-stimulation of a wellbore-to-wellbore permeability volume in low poroperm crystalline rock.

2. MODELLING FRACTURE-TRANSPORT AND PERMEABILITY ENHANCEMENT IN CRUSTAL ROCK

Applying empirical properties (5)-(7) to the thermal energy constraint equations (8) requires representing porosity-permeability spatial correlation at all scales. This can be achieved by finite-element computing of flow/transport/stimulation processes on a single mesh that systematically and coherently supports the spatial-correlation of physical elements of fluid flow and heat transport at all model scales. In the spirit of crustal rock empirics (5) and (7), the domain for fluid flow (6) and associated heat transport (8) is a large-scale numerical mesh of interactive porosity and permeability elements spatially-correlated at all scales and potentially containing spatially-connected long-range flow channels as seen in the lower panels of Fig 2. A 1024-by-1024 node rectilinear grid of spatially-correlated porosity fluctuations represents three decades of scale length spanning, say, 10cm elements in a 100m by 100m crustal section or 3cm elements in a 30m-radius interwell section. Spatially-correlated porosity amplitude fluctuations for such a grid vary over a factor of $32 = \sqrt{1024}$ and correspondingly larger spatial fluctuations in permeability via (5) for values of $\alpha \sim 20$-40 and higher as warranted. Such poroperm grids can be imprinted onto triangular finite-element computation meshes of order 1 million nodes for which wellbore-centric fluid flow constraint equation (6) can be solved by finite-element procedures. Time-evolution of advective heat transfer constraint equation (8) can be solved for fluid flow transport processes expressed on sparser meshes of perhaps 200 to 300 nodes on a side; heat conduction tends to diffuse temperatures over small-scale spatial fluctuations.

Using a single spatially-correlated computational mesh domain, we can implement fundamental empirical spatial correlation scaling (7) with exponent $\beta \sim 1$ for a range of porosities φ and poro-connectivity parameters α. Our first application, termed MWX for 'multiwell experiment', involves fracture-borne fluid heat transport in a sandstone crustal volume transected by a wellbore (Lorenz 2012). Modelling focuses on wellbore-centric fluid flow and heat transport in an individual fault, with thermal effects on the fault diffusing away from the fault into the embedding crustal medium. A fault is taken to be planar crustal section represented by a single 2D mesh centered on the wellbore. The embedding crustal sandstone volume has observed ambient well-core porosity $0.1 < \varphi < 0.3$ and associated poro-connectivity parameter $\alpha \sim 24$. Fault poroperm properties are modelled as having higher porosities as given by well-log porosity data and by higher poro-connectivity parameter values $\alpha \sim 50$-80.

In our second application, termed EGS as representing crustal permeability stimulation of basement rock, we assume that rock volumes contain fossil or relic spatially-correlated poro-connectivity structures with ambient well-core porosity $\varphi < 0.01$ and poro-connectivity parameter $\alpha \sim 300$ as observed in the KTB deep well (http://www-icdp.icdp-online.org/sites/ktb/welcome.html). We assume stimulation does not proceed to the Fig 3 scenario, but instead occurs via non-volumetric shear slip on localised relic flow structures that locally increase α, and hence permeability, without affecting porosity.

In a single-mesh domain, fractures are represented by geometric structures of enhanced porosity and poro-connectivity parameter that do not require the separate meshing commonly employed for standard fault representation. Fractures expressed as enhanced porosity structures embedded in a single mesh are not restricted to planar geometry. In single mesh representations of spatially-correlated poroperm variability, fracture effects that reflect damage to the pre-existing rock fabric can be realised across a spectrum of broader and more diffuse poroperm structures. In particular, single mesh representation of an ambient poroperm medium can seamlessly represent either extended flow structures or localised sites at which fluid pressurisation enhances permeability through increased poro-connectivity parameter α. We are thus able to model a range of crustal fluid flow/transport/damage processes via parameters that can be directly related to existing or potential observational data.

By increasing poro-connectivity without increasing porosity, we avoid the heretofore failed Fig 3 stimulation scenario of enhanced permeability via increased porosity. In line with the lower panels of Fig 2, we suppose EGS permeability stimulation occurs along pre-existing spatially-erratic flow structures. Effectively increasing α by shear-strain activation of pre-existing poro-connectivity implies the existence of slip-failure within zones of weakness. Our modelling thus focuses on slip-damage that generates small-scale seismic emissions. Finite-element modelling applied to the spatial complexity of constraint equation (6) enables incorporating into the stimulation process the detection and location of seismic slip events by which to track, validate, and calibrate permeability enhancement.

Because of the complexity of fluid flow mechanics in spatially-heterogeneous crustal rock, our flow/transport modelling is as simple as possible. One or two sources/sinks of fluid flow are embedded in a single poroperm mesh domain characterised by spatial-correlation scaling exponent $\beta \sim 1$. With the model-domain initially at a uniform ambient temperature, the source/sink wellbores inject/accept fluid of a different temperature into or from the poroperm medium. Computations track the progress of fluid flow and heat transport over time for a range of material parameters. Finite-strain damage criteria such as the von Mises stress can model permeability stimulation processes.

Poroperm data controlling the ambient crustal state for the MWX and EGS simulations are shown in Figs 4 and 5. The left-hand plots show well-core poroperm spatial correlation $\delta\varphi \sim \delta\log(\kappa)$ between sample porosities φ the logarithm of the sample permeabilities κ. The right-hand plots show determination of poro-connectivity parameter α for the two poroperm data suites.

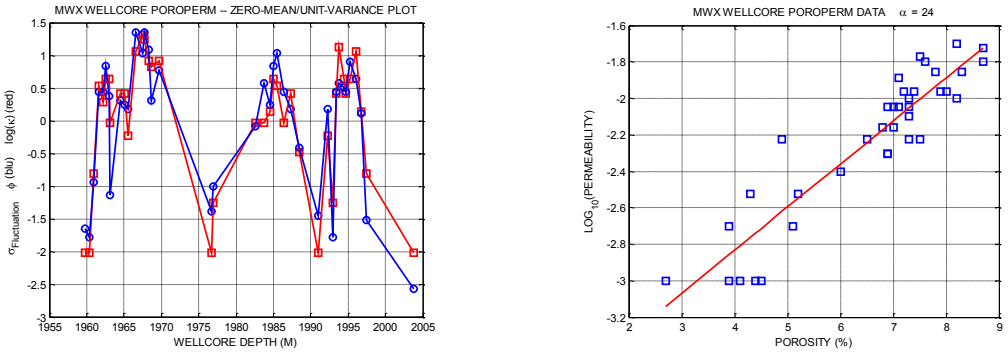

Figure 4: Ambient poroperm properties of MWX tight gas sands for depth interval 1960m to 2005m. (Left) Overlay plot of well-core porosity (blue) and the logarithm of well-core permeability (red); data are reduced to zero-mean/unit-variance format. (Right) Plot of well-core porosity (horizontal axis) against logarithm of well-core permeability (vertical axis); the best-fit slope to the data trend gives the value of the ambient crustal α parameter, $\alpha \sim 24$.

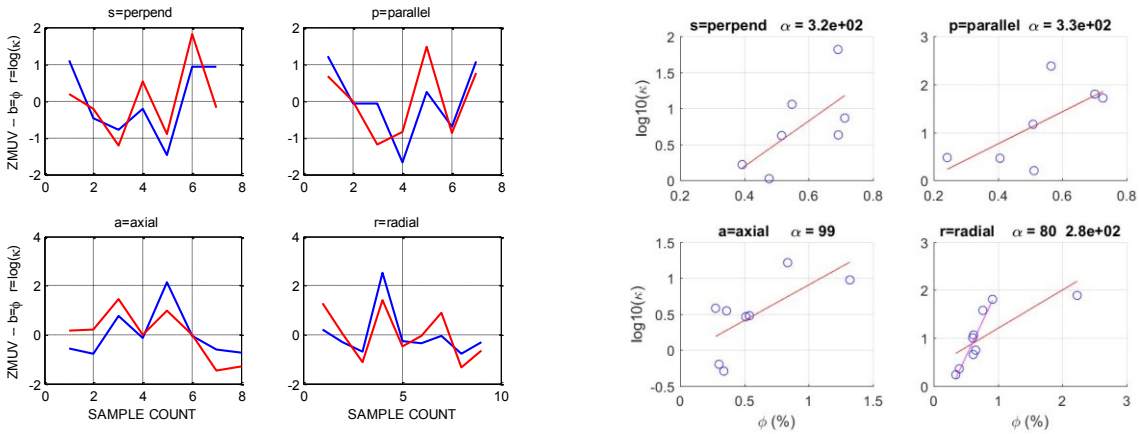

Figure 5: Sample ambient poroperm properties of KTB main-well crystalline basement rock over 4-6km depth interval. (Left) Overlay plots of well-core porosity (blue) and the logarithm of well-core permeability (red); data are reduced to zero-mean/unit-variance format for each of four core orientations; 'perpend' and 'parallel' = perpendicular/parallel to observed fabric; 'axial'/'radial' = along/across the wellbore axis. (Right) Plot of well-core porosity (horizontal axis) against logarithm of well-core permeability (vertical axis) for the four core orientations; best-fit slopes to the data trends give the value of the ambient crustal α parameter, $\alpha \sim 300$ (allowing for a single outlier porosity value for radial sample).

For the MWX simulation of heat advection in a fractured sandstone volume, a wellbore normal to the plane of the fluid-bearing fault accepts hotter fluid from one of the faults. Wellbore-centric heat advection in the fault section determines the evolving thermal structure of the fault plane away from the wellbore. Thermal data acquired in the wellbore normal to the fault plane are due to heat

diffusing into the bounding ambient crust away from the thermally evolving fault plane. For the EGS simulation, a source/sink pair embedded in the computational mesh represent EGS input/outtake wellbores. Wellbore pressurisation creates a stimulation zone between the two wellbores in which α is systematically increased to permit increase interwell flow. For a given level of permeability stimulation, thermal advection computation tracks the evolving thermal structure of the stimulation zone as cold water from the input well forces fluid through the stimulation zone into the outtake well.

2.1 Modelling fracture-borne heat transport in realistic crust rock

Our first modelling step is applied to naturally-occurring wellbore-centric heat advective fluid flow in large-scale fractures. The fractures occur within a crustal volume ~ 200 meters on a side lying between 2.1 and 2.3 km depth in a western Colorado Cretaceous sedimentary sequence of tight gas sands. The tight gas sands were the subject of the extensive MWX hydrofracture investigation (Lorenz 2012). Colorado River erosion gives ~ 850 meters of topographic relief in the vicinity of the MWX project quartet of experimental wellbores. The fluid-conductive/heat-advective nature of the large-scale fractures is signaled by pronounced spikes in the Fig 6 wellbore neutron-porosity logs in company with the Fig 7 sequence of spatially coincident pronounced spikes in the wellbore thermal gradient. A steady-state topographically-driven fluid flow in equilibrium with an ambient crustal temperature field (mean thermal gradient ~ 35°C/km) can be expected to be locally disturbed where the wellbore interests the fractures. Figs 8 and 9 show the spatial relation between porosity and thermal data for the 2100-2300 meter interval with the most prominent flow/thermal signal.

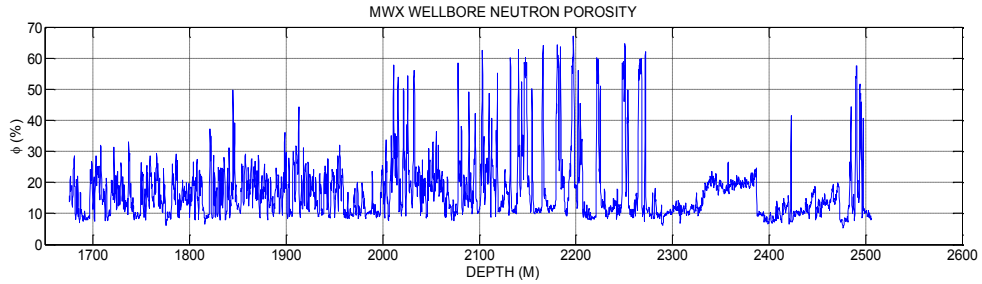

Figure 6: Neutron porosity wellbore log of MXW well between 1675 and 2520 meters.

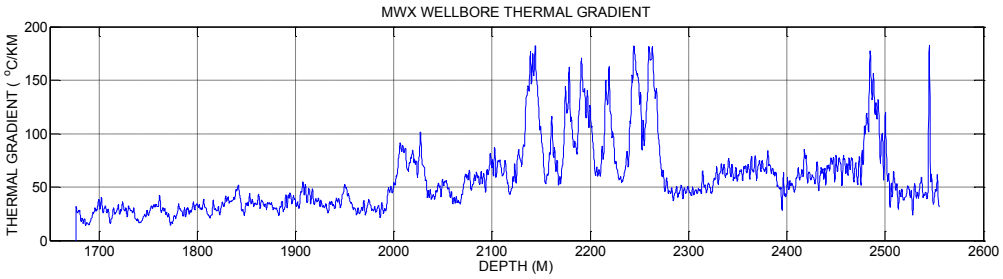

Figure 7: Thermal gradient wellbore log of MXW well between 1675 and 2520 meters.

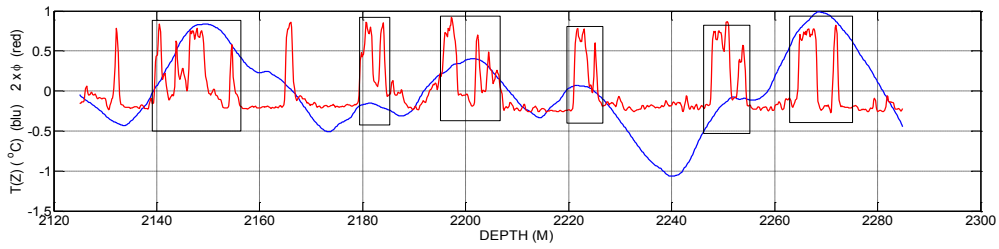

Figure 8: MWX wellbore temperature profile (blue) overlying wellbore porosity profile (red); the porosity data are exaggerated by a factor 2. Temperature maxima occur at the porosity maxima.

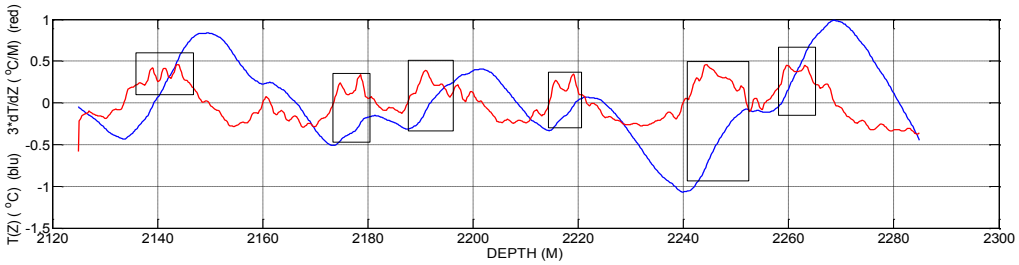

Figure 9: MWX wellbore temperature profile (blue) overlying wellbore temperature gradient profile (red); the amplitude of the gradient field is exaggerated by a factor 3. Temperature gradient maxima lead the temperature maxima by a quarter wavelength.

We focus on the phase and relative amplitude details of the Figs 8-9 wellbore temperature field and its axial gradient. The significant driver of the thermal field is assumed to be disturbance of equilibrium fluid flow and heat advection system by the sudden appearance of a high permeability wellbore. Taking the wellbore as suddenly permitting fluids in a fault to exit at the wellbore, a thermal effect propagates radially into each fault plane as heat-bearing fault fluids move quickly away from the fault to allow fluid of a different temperature to replace the exiting fluid. The time-evolving wellbore-centric advective radial heat transport disturbances within each fracture plane will in turn diffuse normally away from the plane into the ambient crust. The radially-flow driven thermal diffusion signal will register in the wellbore fluid as Figs 8-9 thermal disturbances centered on the location of faults identified by the porosity spikes. The wellbore thermal data thus acts as a proxy for radial heat advection in the fault planes triggered by the sudden appearance of the central wellbore. Fig 10 gives computed radial heat advection curves.

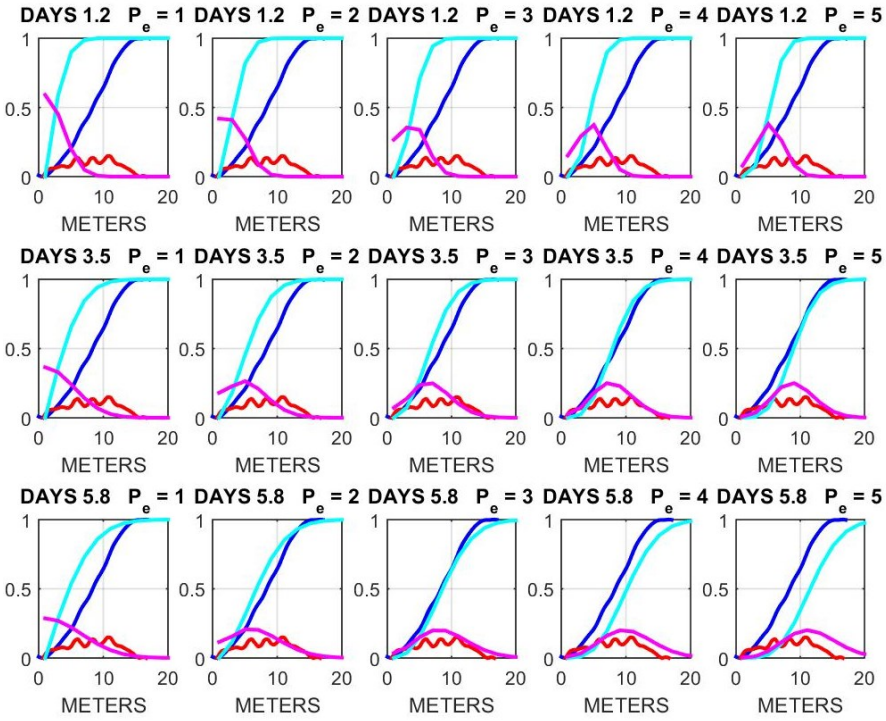

Figure 10: The spatial variation of temperature (blue) and temperature gradient (red) recorded over a 20m interval in the MWX wellbore are matched over 20m wellbore-centric radial interval to give model temperatures (cyan) and temperature gradients (magenta) for a range of radial advection parameters. The model assumption is that radial heat advection temperature distributions in the fracture planes diffuse into the ambient crust normal to the fracture planes. The range of model parameters are three elapsed advection-diffusion times (rows) for five values of wellbore-centric advection Peclet number P_e (columns). The model fits of temperature and temperature gradient distributions indicate that radial flow thermal equilibrium is achieved on the order of 3 to 5 days for radial advective flow Peclet numbers of order 2-3. Heat diffusion away from the fault into the fault-bounding ambient crust occurs over ~ 30 days. For rock-water effective diffusivity $D \sim .7\ 10^{-6}$ m^2/s, the Peclet number for wellbore-centric radial flow $P_e = r_0 v_0 / D$ gives characteristic heat advective fluid flow velocity $v_0 \sim 2\ 10^{-6}$ m/s at characteristic fracture-borne radial dimension $r_0 \sim$ 1m. The pictured model curves are consistent with thermal data from all six the Fig 8-9 fault intervals.

The Fig 10 model radial temperature distributions are computed by solving (8) on a 2D poroperm mesh with spatial correlation property (7) and porosity-mediated permeability (5) via finite-element solution velocity to Darcy flow (6). Models are governed by wellbore-

pressure-induced fluid flow with mean fluid velocity corresponding to values of $P_e = r_0 v_0/D$. The Fig 10 model temperature and temperature gradient overlays are evidence that radial flow heat advection via a natural crustal fracture system can be modeled by flow in a medium meeting the observational empirics (5) and (7). The ambient crust is characterised as having a mean porosity $\varphi \sim 0.1$-0.15 with poro-connectivity parameter $\alpha \sim 24$. Fracture intervals are characterised by higher porosity as measured by the Fig 6 wellbore neutron porosity data, $\varphi \sim 0.3$-0.4, and higher poro-connectivity parameter $\alpha \sim 50$-80 by which to generate suitable permeabilities. The model fits indicate that thermal equilibrium of advected heat is achieved on the order of 3 to 5 days for radial flow Peclet numbers of order 2-3. For the observed spatial scales, thermal diffusion equilibrium in the ambient crust normal to the fracture system occurs over perhaps 30 days. For rock-water effective diffusivity $D \sim 0.7\ 10^{-6}$ m^2/s, the model Peclet numbers for wellbore-centric radial flow $P_e = r_0 v_0/D$ gives characteristic heat advective fluid flow velocity $v_0 \sim 10^{-6}$ m/s at characteristic fracture-borne radial dimension $r_0 \sim 1$m corresponding to $v_0 \sim 10^{-5}$ m/s fluid entry flow at wellbore radius $r_0 \sim 10$cm.

In crustal rock of ambient mean porosity $\varphi \sim 1/2\pi$, fluid flow of Peclet number $P_e \sim 2$-3 into a wellbore over an observed fault interval $\ell \sim 5$m produces wellbore fluid outtake $V = 2\pi\varphi\, r_0 v_0 \ell \sim 2 \cdot 10^{-6} \cdot 5\text{m}^3/\text{s} \sim 10$ml per second across each 5m fracture interval. Each of the observed fracture intervals may be inferred to produce $\sim 1\text{m}^3$ of fluid per day. For a 2km wellbore of volume $\sim 60\text{m}^3$, the rate of fluid flow from the observed fractures replaces the wellbore fluid in two weeks. At such wellbore flow rates, the observable thermal effects of the wellbore disturbance of the ambient steady-state flow/thermal regimes are strictly local to the wellbore-centric fault fluid flow.

Extrapolating the natural fracture-borne fluid flow associated with $P_e \sim 2$-3 from 5m intervals to 1km wellbore intervals, the total fluid production by the wellbore is 2 liters per second. An EGS stimulation project producing 2 liters/second is thus roughly equivalent to achieving crustal stimulations of 200 MWX crustal fractures of 5m thickness and radius ~20 radius for each km of production wellbore.

2.2 Modelling permeability stimulation in realistic crust rock

Fig 10 radial advective heat transport modeling indicates that wellbore fluid flow producing 2 liters/second can be achieved by a km-long sequence of 5m-wide $P_e \sim 2$-3 fracture-connectivity flow pathways as occur naturally in the sandstones transected by the MWX wellbore. We use this model-interpretation of natural flow enhancement as a normative physical basis for considering EGS flow stimulation in basement rock with ambient porosity $\varphi \sim 0.01$, an order of magnitude lower than MWX sandstones.

Our Fig 10 numerical model of naturally-occurring crustal faults attributes higher fluid flow rates to greater porosity of fault intervals, as seen in Fig 4, boosted by model-driven larger poro-connectivity parameter α due to greater poro-connectivity within a fault. Fig 5 poroperm data for KTB basement rock show a natural occurrence of increased α as a physical means of increased permeability without increasing porosity: KTB rock of low porosity $\varphi \sim 0.01$ is accompanied by high poro-connectivity parameter $\alpha \sim 300$. A plausible interpretation of the MWX → KTB poroperm data trend is that increasing flow by increasing porosity requires doing work against gravitational compressive stress to a much greater degree than does increasing flow by increasing α. A mechanical interpretation of increasing permeability by increasing α is that finite-strain grain-scale damage via non-volumetric shearing increases flow links between existing pores without the need of creating new pore space. Non-volumetric shearing damage may thus be logically inferred to be energetically favoured by increasing the poro-connectivity, hence permeability, without the energy-penalty of work against compressive stress. Prompted by Fig 5 poroperm data and the energy-efficiency argument, we model EGS stimulation of wellbore-to-wellbore fluid flow in a low-porosity poroperm medium $\varphi \sim 0.01$ by increasing the KTB poro-connectivity parameter $\alpha \sim 300$ to $\alpha \sim$1000-1500. We note in passing that values of $\alpha > \sim 1500$, i.e. values of $\alpha\varphi > \sim 15$, can encounter numerical stability problems.

KTB well-log data support EGS stimulation via increased α as reflecting non-volumetric physical processes for increasing rock permeability. Neutron scattering in KTB well-logs returns apparent porosity values $\varphi_{log} \sim 0.1$ that are an order of magnitude greater than Fig 5 well-core data, $\varphi_{core} \sim 0.01$. KTB well-logs in general show, however, that (i) the amplitude of spatial fluctuations in rock properties does not diminish with increasing depth, and (ii) spectral scaling (7) of rock property spatial fluctuations remains unchanged with depth. It appears that increasing confining stress does not homogenize rock so much as force pore waters into hydrated minerals deposited in the fracture-connectivity pathways inherited from fracture-pathways active at shallower depths and in less consolidated or metamorphosed rock. We can infer from well-log data that depth-independent neutron scattering occurs at water of hydration in fossilized flow channels that preserve spectral-scaling fluctuation-power scaling (7) at drillable crustal depths. The Fig 4-5 parallels between MWX and KTB rock poroperm properties and the attested existence of fossil fracture-connectivity spatial-correlation pathways validate our modelling approach to EGS stimulation of basement rock.

Following the Fig 10 finite-element time-evolving solutions (8), we model wellbore-centric fluid flow in basement rock terms of a poroperm medium but for new values of poroperm parameters, lower porosity $\varphi \sim 0.1 \rightarrow 0.01$ but higher poro-connectivity $\alpha \sim 24 \rightarrow \alpha \sim 300$ for ambient rock and increasing to $\alpha \sim$ 1000-1500 for stimulated rock. Beginning with an isothermal model domain for given poroperm parameters, cold water enters the medium at one wellbore and displaces hot water into a second wellbore. The sequence of advection/diffusion temperature fields evolve according to (8). Fig 11 shows the results of such modelling.

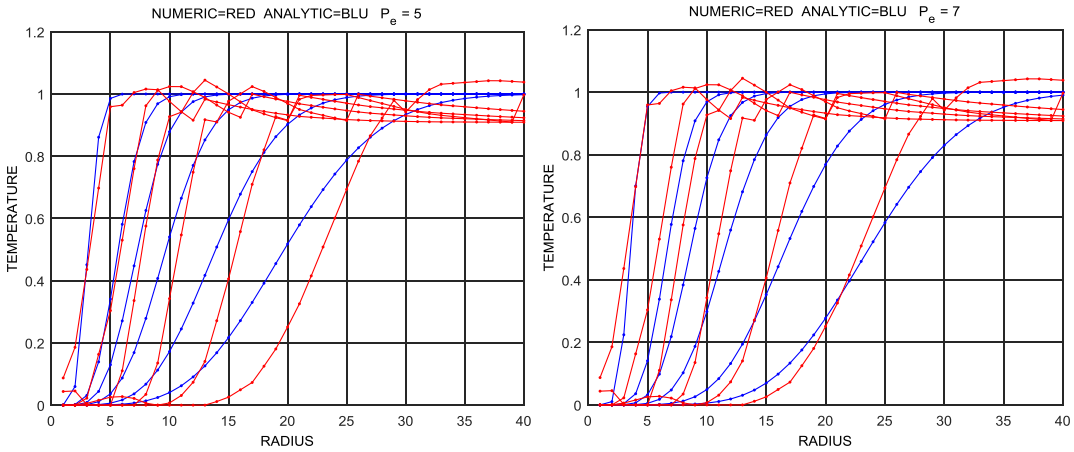

Figure 11: Time-evolving radial temperature profiles for finite-element model computations (red) and analytic expression (11) (blue). Model computations control effective radial flow Peclet number by the value of the poro-connectivity parameter α that determines the rate of fluid flow in the stimulation volumes between wellbores. For sufficiently large values of α flow-connectivity between EGS wellbores creates an equivalent Peclet number 5-7 heat transfer from the crustal volume into the outtake wellbore.

As no field data exist for comparison with the model, Fig 11 compares model wellbore-centric advective flow temperature curves in red to curves in blue computed for the Carslaw & Jaeger wellbore-centric heat advective flow analytic expression (11). Time-evolution sequences in Fig 11 show the radial distribution of temperature in hot rock into which cold water steadily flows to cool the surrounding rock. Beginning at early times and small radii at the left of the plots, the continuous wellbore-centric advective flow cools the medium according to sequence of curves from left to right. The rightward drift of curves shows the changing shape of the radial temperature distributions as cold water from the wellbore continues to penetrate the surrounding rock.

In the wellbore-to-wellbore model flow scenario, introduction of cold water at one wellbore pushes hot water from the surrounding rock into the second wellbore at rates corresponding to the Peclet number of the flow model. Model Peclet numbers are determined by the values of the model poro-connectivity parameter α. The values of the Peclet numbers for the model computations are validated by matching the model temperature curves in red to temperature curves in blue computed for analytic single-wellbore advective flow expression (11). The numerical and analytic curves are approximate because of the different flow geometries. More exact comparisons between numeric and analytic expressions await detailed computations on finer numerical meshes.

3. DISCUSSION/CONCLUSIONS

There has been to date little practical success with EGS extraction of crustal heat via treating rock as an effectively quasi-homogeneous elastic continuum in which planar fractures can be stimulated as, in the words of Tester et al (2006), "a series of flat plates with gaps (the fractures) between them [and heat] transferred by conduction...perpendicular…to the fractures". A quasi-homogeneous crust reduces the conservation of fluid mass constraint equation to a convenient and computationally tractable constraint on fluid pressure, $\nabla^2 P = 0$. Flow modelling solutions to $\nabla^2 P = 0$ require only a small number of rock parameters to enforce geometric boundary conditions on the pressure field. Solution to the conservation of thermal energy constraint equation (8) is correspondingly simplified. Quasi-homogeneous media thus spawn a computational bias towards coarse meshes for large-scale quasi-uniform rock components requiring few rock parameters and dense meshes for fluid flow in thin fracture-gaps between the rock components. Sparse meshing of quasi-uniform crustal blocks also allows for modelling Hm-scale crustal volumes consistent with physical dimensions supporting long-duration/high-Peclet-number flow required for electricity generation.

In light of continued failure of the effective medium continuum approach to EGS, we note that there is no observational basis for a quasi-homogeneous continuum approximation to rock. There is instead a great deal of well-log, well-core, and well-production data attesting to highly heterogeneous fluid flow at all scales within the crust. The observed spatial heterogeneity of crustal flow processes fundamentally amends the conservation of fluid mass constraint equation to include spatial heterogeneity in porosity $\varphi(x,y)$ scaled by a large physically and computationally significant empirical poro-connectivity parameter α, $\nabla^2 P + \alpha \nabla\varphi \cdot \nabla P = 0$. This 'real crust' fluid flow constraint equation, and the corresponding thermal energy conservation constraint equation, must be solved at all scales simultaneously to allow for the unpredictable spatially-erratic fracture-connectivity flow paths inherent in the crust. Accordingly, flow and transport computation involves large numbers of stochastic flow properties distributed heterogeneously throughout the computational volume. To accomplish this task, computational methodology must allow for stochastic arrays realised on a single support mesh of essentially uniform density throughout the model. Finite-element computation is fundamentally suited to this task.

We find that finite element computation can provide physically reasonable, if presently crude, approximations to thermal energy transport in highly heterogeneous spatially-correlated stochastic flow media defined by crustal-flow empirical parameters that control spatial correlation and poro-connectivity. For fractured sandstones of moderate porosity $\varphi \sim 0.1$-0.15 and poro-connectivity parameter $\alpha \sim 24$, finite-element modelling of time-evolving wellbore-centric heat transfer in large-scale fractures of observed porosity $\varphi \sim 0.3$-0.4

and hypothetical $\alpha \sim 50\text{-}80$ reproduces the associated wellbore temperature field for radial advection Peclet numbers $P_e \sim 2\text{-}3$. Using the generic nature of crustal rock empirics, we find we can plausibly shift from standard sandstones to tight crystalline basement rock with $\varphi \sim 0.01$ and $\alpha \sim 300$ to model wellbore-to-wellbore flow in a hypothetical EGS stimulation volume characterised by poro-connectivity $\alpha \sim 1000\text{-}1500$. Time-evolving thermal transport computation between wellbores indicates that model temperature profiles are roughly equivalent to radial advection Peclet number $P_e \sim 5\text{-}7$ for the analytic solution to wellbore-centric advective flow into a uniform medium.

Our Fig 10-11 modeling for two distinct instances of fluid flow empirical poroperm media have the same order of radial flow Peclet number. Despite an order of magnitude difference in ambient porosity and characteristic poro-connectivity parameter α, Fig 11 hypothetical EGS physical stimulation process Peclet numbers, $P_e \sim 5\text{-}7$, are of the same order as Fig 10 model Peclet numbers, $P_e \sim 2\text{-}3$, matched to temperature data in the MWX natural fracture-borne advective flow system. Wellbore-centric fluid flow in empirically constrained MWX and EGS poroperm media have Peclet numbers that appear to be fundamentally constrained in magnitude. Our present modelling results can be considered compatible with naturally-convecting geothermal flow systems that probably achieve $P_e \sim 100$ flow rates in poroperm media by combining high porosity with high poro-connectivity within large-scale tectonically generated fracture-borne flow systems. Our constrained Peclet numbers may, in contrast, have strong implications for EGS stimulation that can achieve the order-of-magnitude higher Peclet numbers implied by traditional Fig 3 concepts of heat extraction from low porosity rock.

We note that the currently failed Fig 3 EGS scenario depends on 'pipe-flow' rather than 'poroperm medium flow'. It may be further noted that Darcy's law emerged when Darcy and Dupuit recognised that their 'pipe flow' concepts of groundwater flow were incorrect (Brown 2002). The physically accurate description of groundwater flow was recognised after Darcy's close observation of groundwater flow rates in relation to groundwater pressure-heads. A second generation of careful observation and modelling of the details of fluid flow in rock may be required to set realistic EGS goals. The conceptual/physical difference between 'pipe-flow' and 'poroperm medium flow' is profound, and may be decisive for the future of EGS heat energy extraction.

Several conclusions emerge from our finite-element solutions for flow/transport on suitably heterogeneous poroperm media:

- The inherent spatial heterogeneity of crustal rock flow requires a fundamental rethink of what is possible to achieve with currently available EGS stimulation techniques.
- Well-log, well-core, and well-production data for sandstone and basement rock merge into a conceptual/computational poroperm spectrum for application to EGS stimulation.
- Poroperm properties porosity φ and poro-connectivity parameter α may represent rock permeability via different finite-strain deformation processes: φ controlled by volumetric compression and α controlled by non-volumetric shear.
- Finite-element computation can satisfactorily meet the flow/transport modelling task if defined on a single mesh spanning the entire model flow/transport/stimulation volume.
- Physically accurate finite element transport/flow modelling can be integrated with detailed seismic observation of wellbore-centric EGS shear-strain stimulation in order to better understand the physics of crustal flow stimulation.
- Present modelling estimates of wellbore-centric Peclet number flow/transport – naturally-occurring fracture flow system $P_e \sim 2\text{-}3$ and hypothetical stimulation of wellbore-to-wellbore flow $P_e \sim 5\text{-}7$ – suggest that natural rock properties present a barrier to the achieving the order-of-magnitude higher Peclet numbers required for power generation.
- Given the current need to generate EGS stimulation via wellbore pressurisation, traditional EGS concepts based on fluid flow in 'pipes' rather than in 'poroperm media' may be fundamentally unrealizable.

ACKNOWLEDGEMENTS

The Matlab finite element Partial Differential Equation Toolbox™ provides a powerful and readily accessible means to solve the conservation of mass and thermal energy constraint equations for highly heterogeneous poroperm flow media characterised by spatial correlations at all scales. We are deeply grateful to Antti Hannukainen and Tuomo Kuusti, Aalto University, for extending the Matlab modelling facility to time-evolving advective flow (Antti) and for support discussions on the mathematics of diffusion processes on spatially-correlated structures (Tuomo). We also benefitted from ongoing discussions with Ilmo Kukkonen, University of Helsinki, and Maren Brehme, Guido Bloecher, Mauro Cacace, Harald Milsch, Ernst Huenges, and Gunter Zimmermann of GFZ-Potsdam. We thank Ronald Conze and Uli Harms, ICDP, for access to KTB main hole well-log and well-core data.

REFERENCES

Banks D, Gundersen P, Gustafson G, Mäkelä J & Morland G (2010) Regional similarities in the distributions of well yield from crystalline rocks in Fennoscandia, *Norges geologiske undersøkelse Bulletin* 450, 33–47.

Bachmat Y & Bear J (1987) On the concept and size of a representative elementary volume (REV), *Advances in Transport Phenomena in Porous Media* editors: J Bear & M Y Corapcioglu, 1987 Martinus Nijhoff Publishers Dordrecht / Boston / Lancaster

Bear J (1972) *Dynamics of fluids in porous media,* American Elsevier, New York.

Biot MA (1941) General theory of three-dimensional consolidation, *Journal of Applied Physics* 12, 155-164.

Brown GO (2002) Henry Darcy and the making of a law, *Water Resources Research* 38, No 7, 1-12.

Carslaw HS & Jaeger JC (1959) *Conduction of Heat in Solids*, Clarendon Press, Oxford, pp510.

Cladouhos TT, Petty S, Nordin Y, Moore M, Grasso K, Uddenberg M, Swyer M, Julian B & Foulger G (2013) Microseismic monitoring of Newberry volcano EGS demonstration, 38th Workshop on Geothermal Reservoir Engineering Stanford University, SGP-TR-198.

Costanza-Robinson MS, Estabrook BD & Fouhey DF (2011) Representative elementary volume estimation for porosity, moisture saturation, and air-water interfacial areas in unsaturated porous media: Data quality implications, *Water Resources Research* Vol 47, W07513.

Darcy H (1856) *Les Fontaines publiques de la ville de Dijon*, Victor Dalmont, Paris.

de Wiest R (1961) On the theory of leaky aquifers, *Journal of Geophysical Research* Vol 66 No 12, 4257-4262.

de Wiest R (1966) On the storage coefficient and the equations of groundwater flow, *Journal of Geophysical Research* Vol 71 No 4, 1117-1122.

de Wijs HJ (1951) Statistics of ore distribution. Part I: frequency distribution of assay values, *J. R. Neth. Geol. Min. Soc*. New Ser.13, 365–375.

de Wijs HJ (1953) Statistics of ore distribution Part II: theory of binomial distribution applied to sampling and engineering problems, *J. R. Neth. Geol. Min. Soc*. New Ser. 15, 125–124.

Dupuit J (1863) *Etudes Theoriques et Pratiques sur le Mouvement des Eaux dans les Canaux Decouverts et a Travers les Terrains Permeables*, 2nd ed., Dunod, Paris.

Earlougher RC (1977) *Advances in Well Test Analysis*, Society of Petroleum Engineers, Dallas, pp264.

Freeze RA (1975), A Stochastic-Conceptual Analysis of One-dimensional Groundwater Flow in Non-uniform Homogeneous Media, *Water Resources Research* 11, 725-741.

Geiser P, Lacazette A & Vermilye J (2012) Beyond 'dots in a box': an empirical view of reservoir permeability with tomographic fracture imaging, *First Break* 30, p. 63-69.

Gelhar LW (1986) Stochastic subsurface hydrology from theory to applications, *Water Resource Research* 22, 135S-145S.

Gringarten AC & Witherspoon PA (1973) Extraction of Heat from Multiple-Fractured Dry Hot Rock, *Geothermics* 2, No. 3-4, 119-122.

Gustafson G (2002) Strategies for groundwater prospecting in hard rocks: a probabilistic approach, *Norgesqeoloqiske undersøkelse Bulletin* 439, 21-25.

Hantush MS & Jacob CE (1954) Plane potential flow of ground water with linear leakage, *Transactions American Geophysical Union*, Vol 35, 917-936.

Hasting M et al (2011) Real-time induced seismicity monitoring during wellbore stimulation at Paralana-2 South Australia, *Australian Geothermal Energy Conference 2011,* 85-102.

Hjelmstad KD (2005) *Fundamentals of Structural Mechanics*, Springer, New York, pp480.

Horner DR (1951) Pressure build-up in wells, In: *Third World Petroleum Congress*, The Hague, pp 503-523.

Hubbert MK (1940) The theory of ground-water motion, *Journal of Geology* 48, No 8 Part 1, 785:944.

Hubbert MK (1941) *Transactions of the New York Academy of Sciences*, Series II No 3, 39-55.

Hubbert MK (1957) Darcy's law and the field equations of the flow of underground fluids, *International Association of Scientific Hydrology*, Bulletin 2:1, 23-59, DOI: 10.1080/02626665709493062.

Hubbert MK & Willis DG (1957) Mechanics of Hydraulic Fracturing, *Transactions Society of Petroleum Engineers AIME* 210, 153-168.

Hughes TJR (2000) *The Finite Element Method*, Dover Publications, New York, pp682.

IEA (2012) Special Report: Golden Rules for Golden Age of Gas, *International Energy Agency*, www.iea.org; http://www.iea.org/publications/ freepublications/publication/WEO2012_GoldenRulesReport.pdf, 150p.

IFC (2013) *Success of Geothermal Wells: A global study*, International Finance Corporation, Washington DC, 80pp.

Ingebritsen S, Sanford W & Neuzil C (2006) *Groundwater in Geological Processes*, Cambridge University Press, pp536.

Jacob CE (1946) Radial flow in a leaky artesian aquifer, *Transactions American Geophysical Union* Vol 27, 198-205.

Krige DG (1981) Lognormal-de Wijsian Geostatistics for Ore Evaluation, South African Institute of Mining and Metallurgy, Johannesburg, pp51.

KTB/ICDP http://www-icdp.icdp-online.org/sites/ktb/welcome.html

Law J (1944) A statistical approach to the interstitial heterogeneity of sand reservoirs, Technical Publication 1732, *Petroleum Technology* 7, May 1944.

Leary PC (1991) Deep borehole log evidence for fractal distribution of fractures in crystalline rock, *Geophysical Journal International* 107, 615-628.

Leary PC (1997) Rock as a critical-point system and the inherent implausibility of reliable earthquake prediction, *Geophysical Journal International* 131, 451-466.

Leary PC (2002) Fractures and physical heterogeneity in crustal rock, in *Heterogeneity of the Crust and Upper Mantle – Nature, Scaling and Seismic Properties*, JA Goff & K Holliger eds., Kluwer Academic/Plenum Publishers, New York, 155-186.

Leary PC & Al-Kindy F (2002) Power-law scaling of spatially correlated porosity and log(permeability) sequences from northcentral North Sea Brae oilfield well core, *Geophysical Journal International* 148, 426-442.

Leary P, Malin P, Geiser P, Pogacnik J, Rugis J & Valles B (2015) Flow Lognormality & Spatial Correlation in Crustal Reservoirs: I – Physical Character & Consequences for Geothermal Energy, WGC2015, 19-24 April, Melbourne AU.

Lorenz JC (2012) MWX - The Multiwell Experiment in the Piceance Basin, Colorado: Reprise from 30 Years Ago, AAPG Search and Discovery Article #70129.

Malin P, Leary P, Shalev E, Rugis J, Valles B, Boese C, Andrews J & Geiser P (2015) Flow Lognormality and Spatial Correlation in Crustal Reservoirs: II – Where-to-Drill Guidance via Acoustic/Seismic Imaging, WGC2015, 19-24 April, Melbourne AU.

Muskat M (1937) *The Flow of Homogeneous Fluids Through Porous Media*, McGraw-Hill, pp763.

Nordahl K & Ringrose P (2008) Identifying the representative elementary volume for permeability in heterolithic deposits using numerical rock models, *Mathematical Geosciences*, 40:753–771.

Parker RH (1989) *Hot Dry Rock Geothermal Energy*, Pergamon Press, Oxford, Vol 2: 683-740.

Pogacnik J, Leary P, Malin P, Geiser P, Rugis R & Valles B (2015) Flow Lognormality and Spatial Correlation in Crustal Reservoirs: III – Natural Permeability Enhancement via Biot Fluid-Rock Coupling at All Scales, WGC2015, 19-24 April, Melbourne AU.

Shapiro SA & Dinske C (2009) Fluid-induced seismicity: Pressure diffusion and hydraulic fracturing, *Geophysical Prospecting* 57 301-310.

Tester JW et al. (2006), *The Future of Geothermal Energy -- Impact of Enhanced Geothermal Systems (EGS) on the United States in the 21st Century*, Massachusetts Institute of Technology, pp372 http://geothermal.inel.gov.

Tester JW, Brown DW & Potter RM (1989) Hot Dry Rock Geothermal Energy--a New Energy Agenda for the 21st Century, Los Alamos National Laboratory report LA-1 15 14-MS, Los Alamos, NM.

Theis CV (1935) *Transactions of the American Geophysical Union,* Part 2, 519-524, August 1935.

US Energy Information Administration (2011) *Distribution and Production of Oil and Gas Wells by State*, www.eia.gov/pub/oil_gas/petrosystem/all-years-states.xls.

Warren JE & Skiba FF (1964) Macroscopic dispersion, *Society of Petroleum Engineers Journal* SPE648, 215-230.

Warren JE & Root PJ (1963) The Behavior of Naturally Fractured Reservoirs, *Society of Petroleum Engineers Journal* SPE426, 245-255.

Wunder R & Murphy H (1978) Thermal drawdown and recovery of singly and multiply fracture hot dry reservoirs, *Report LA-7219-MS*, Los Alamos National Laboratory, 15pp.

Yeh TC & Stephens DB (1988) A review of the scale problem and applications of stochastic methods to determine groundwater travel time and path, Daniel B Stephens & Associates Inc, Socorro NM, pp502; www.nrc.gov/docs/ML0327/ML032740229.pdf